ORIGINAL PAPER

Correlations of Composition, Structure, and Hardness in the High-Entropy Alloy System Nb–Mo–Ta–W

Bin Xiao[1] · Yury Lysogorskiy[2] · Alan Savan[1] · Heidi Bögershausen[3] · Janine Pfetzing-Micklich[4] · Dierk Raabe[3] · Ralf Drautz[2] · Alfred Ludwig[1]

Abstract

Refractory high-entropy alloys are of interest due to the potential of compositionally complex alloys to achieve combinations of mechanical properties such as room-temperature ductility and high-temperature strength rarely found in simpler alloys. To study a large compositional range of the system Nb–Mo–Ta–W, thin-film materials libraries were fabricated by combinatorial sputtering. High-throughput characterization methods were used to systematically determine composition-dependent properties: (I) the extent and stability of the complex solid solution range and (II) the mechanical properties (Young's modulus, hardness). The whole investigated composition range of $Nb_{20–59}Mo_{9–31}Ta_{10–42}W_{12–32}$ crystallized in a bcc phase, independent of annealing temperatures ranging from 300 to 900 °C. Mechanical strength values of the Nb–Mo–Ta–W compositions were calculated using the Maresca–Curtin analytical model parameterized with experimental data. A strong positive correlation with measured hardness was observed that allows using this analytical model for optimization of the mechanical strength. We predict that compositions with high Mo contents provide the highest hardness values.

Keywords High-entropy alloys · Hardness · Nanoindentation · Combinatorial synthesis · High-throughput characterization

Introduction

Metallic materials are subject of extensive research due to their scientific and industrial potential. Owing to the fast development of new technologies and theories, the traditional alloy concept has been expanded to high-entropy alloys (HEAs) [1]. Compared to traditional alloys based on one primary metal with small quantities of others, HEAs generally contain at least four metals mixed in approximately equal proportions. The large composition space and the remarkable features exhibited by HEAs make them candidates for a variety of applications.

Much of the interest in HEAs for mechanical purposes arises from their exceptional high-strength and high-temperature tolerance capabilities [2]. Early-reported HEAs based on Al, Co, Cr, Cu, Fe, Mn, Ni, and Ti demonstrate outstanding mechanical properties that have caught up with those of some steels [3]. For example, the yield stress, fracture strength, and plastic strain for $AlCoCrFeNiTi_{0.5}$ HEAs surpass most high-strength alloys [4]. The introduction of refractory high-entropy alloys (RHEAs) by Senkov et al. has pushed the physical and mechanical performance of these alloys to a new level. RHEAs, composed of extremely high melting temperature (up to 3500 °C) refractory elements, e.g., Nb, Mo, Ta, W, Hf, Zr, and Ti, were reported to have superior strength [5], good tribological performance [6], and improved thermal stability [7–9]. As an outstanding example of RHEAs, equiatomic Nb–Mo–Ta–W demonstrates great microstructural stability and could maintain high hardness after exposure to 1400 °C [5].

✉ Alfred Ludwig
alfred.ludwig@rub.de

1   Chair for Materials Discovery and Interfaces, Institute for Materials, Faculty of Mechanical Engineering, Ruhr University Bochum, Universitätsstr. 150, 44780 Bochum, Germany

2   Chair of Atomistic Modelling and Simulation, Interdisciplinary Centre for Advanced Materials Simulation (ICAMS), Ruhr University Bochum, Universitätsstr. 150, 44780 Bochum, Germany

3   Max-Planck-Institut für Eisenforschung GmbH, Max-Planck-Straße 1, 0237 Düsseldorf, Germany

4   ZGH, Ruhr University Bochum, Universitätsstr. 150, 44780 Bochum, Germany

Nb–Mo–Ta–W was first prepared in bulk form by vacuum arc melting [5]. Recently, also Nb–Mo–Ta–W thin films were produced, which exhibit high hardness and high thermal stability, thus showing potential to be used as a coating material and diffusion barrier [10, 11]. Nb–Mo–Ta–W crystalizes as a disordered body-centered cubic (bcc) solid solution. Its mechanical properties and thermal stability can be tuned by substitution of heavy elements with lighter ones (Hf, Zr, and Ti) [12, 13] or adding metallic (Al or Cr) [14, 15] and non-metallic elements (C or O) [16]. For instance, upon substituting Mo and W with Ti and Zr, a significant increase of the compression strain, up to 40% at room temperature, was reported in the system Ta–Nb–Hf–Zr–Ti [17]. Moving farther in this direction, a large number of compositional derivatives, deviating from the equiatomic composition, were reported [18]. Superior hardness (ranging from 689 to 892 HV) and enhanced compression strength of 1630 MPa were observed in oxygen- and carbon-incorporated non-equilibrium Nb–Mo–Ta–W [19].

However, up to now, no detailed study regarding how compositions affect the phase(s) and properties of the solid solution is reported. Understanding the relevant mechanisms is needed to guide design and optimization of RHEAs with desired properties and establish the compositional margins and tolerances to retain them. Therefore, an Nb–Mo–Ta–W thin-film materials library, covering a wide compositional range of $Nb_{20-59}Mo_{9-31}Ta_{10-42}W_{12-32}$, was fabricated by combinatorial magnetron co-sputtering from four elemental sources. We present and discuss their chemical, structural, and mechanical properties, with a focus on investigation of their hardness values. The aim is to correlate the compositional variation with mechanical properties of RHEAs. We show that the development of functional materials can be accelerated by integration of combinatorial synthesis, high-throughput experimentation, and computational modeling.

Materials and Methods

Analytical Model for Mechanical Strength of RHEA

The reduced Maresca–Curtin solid solution model for the calculation of the uniaxial yield strength in bcc RHEAs was used to study trends in mechanical properties [20]. For a given composition, the model requires as input: lattice constant a, elastic moduli C_{11}, C_{12}, and C_{44}, and the misfit volumes ΔV_j of the constituent elements, which we took from Ref. [21]. We applied basic approximations, such as rule of mixtures and Vegard's law, to estimate values of elastic moduli, lattice constants, and atomic volume mismatch [22]. In Ref. [20] the validation of the proposed full model for RHEAs composed of Mo, Nb, Ta, W, and V was performed with respect to molecular dynamics simulations as well as to

experimental measurements. The reduced model that is feasible for high-throughput screening was also compared to the full model and agreement within 5% was demonstrated. Of course, there are clear limitations of both models, because they do not include short-range ordering, segregation onto defects, and polycrystallinity. In the current work the predictions of the reduced Maresca–Curtin model are considered as proxy properties for materials strength optimization. For the yield strength optimization we did not limit the composition range, except for a minimum content of 5 at.% for each element in order to maintain a four-component RHEA alloy.

## Synthesis of Nb–Mo–Ta–W Thin-Film Materials Library

A Nb–Mo–Ta–W thin-film materials library (ML) was fabricated using a combinatorial magnetron sputter system (DCA Instruments, Finland) by co-deposition from four confocal elemental targets on a stationary substrate, leading to four well-defined compositional gradients. High-purity (Nb: 99.99%, Mo: 99.9%, Ta: 99.99%, W: 99.99%) 100-mm diameter Nb, Mo, Ta, and W targets were used. Each target was positioned with an inclination angle of around 45° with respect to the substrate, as indicated in Fig. 1a. A detailed description of this sputter system can be found in Ref. [23]. The deposition was carried out without intentional heating. Due to particle bombardment during sputtering, the substrate temperature could reach to around 70 °C. A 100-mm diameter sapphire wafer (c-plane) was used as substrate. It was patterned with small numbered crosses by a photolithographic lift-off process. Each patterned number is assigned to a measurement area (MA), defined in a grid area with size of 4.5 mm × 4.5 mm. There are in total 342 MAs in a ML, arranged in a 20×21 matrix (see Supporting Information). Prior to the deposition, the chamber vacuum was on the order of 10^{-5} Pa. During deposition, the pressure was set to 0.667 Pa of Ar (99.9999%), and the substrate was kept stationary to obtain four continuous compositional gradients. The type of power supply used for each target and sputter powers are listed in Table SI1. After deposition, the photoresist was removed in an ultrasonic bath.

High-Throughput Characterization of Nb–Mo–Ta–W Thin-Film Materials Library

The ML was characterized by a series of high-throughput methods, including energy-dispersive X-ray spectroscopy (EDS) for composition, X-ray diffraction (XRD) for phase constitution, atomic force microscope (AFM) for roughness, and nanoindentation for Young's modulus and hardness.

The elemental compositions were determined using automated EDS, conducted on a JEOL 5800 scanning electron microscope (SEM). A 20-kV accelerating voltage, 10-mm

Fig. 1 Schematic visualization of the combinatorial co-sputter process for the synthesis of the quaternary composition spread thin-film MLs. **a** Confocal magnetron sputter cathode arrangement for the co-deposition of Nb–Mo–Ta–W MLs. **b** Pie chart diagram indicating the relative elemental compositions at each of the 342 MAs. The legend shows the locations of elements

(a)

(b)
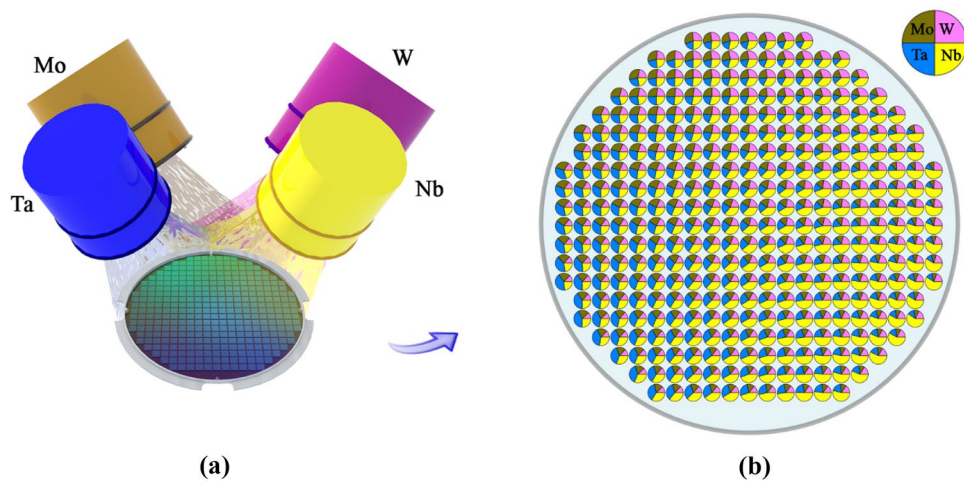
working distance, and a magnification of ×600 with acquisition times of 60 s for each MA were used during the measurement. The analysis of EDS data was performed based on the standard ZAF correction process provided by the INCA Energy software (Oxford Instruments). The software was calibrated for quantification using a Co standard.

High-throughput phase analysis was done using XRD (Bruker D8 Discover, equipped with a VANTEC-500 area detector, Cu Kα radiation, with a sample-to-detector distance of 149 mm). The X-ray beam size was collimated to 1 mm (collimator diameter = 1 mm with a divergence < 0.007°). An area detector was used, and 3 frames were collected for each measured area to cover the 2θ range from 15° to 80°. The total time for XRD measurements for one ML with 342 measurement areas was 20 h. The raw data were compiled and integrated into one-dimensional datasets using DIF-FRAC.EVA software provided by Bruker. A Python script was used to automate the process. The phases were identified by comparing the measured patterns with references from the Inorganic Crystal Structure Database (ICSD). The lattice constants of the films in the ML were determined using Bragg's law. The lattice spacing of (110)-oriented films and the equivalent lattice constant of a cubic crystal can be calculated using Eqs. (1) and (2):

$$d_{hkl} = \frac{n\lambda}{2\sin\theta}, \tag{1}$$

$$a, b, c = d_{hkl}\left(h^2 + k^2 + l^2\right)^{1/2}, \tag{2}$$

where n, d, and θ represent positive integer, interplanar spacing, and the angle between the adjacent crystal planes, respectively. Among analytical techniques applied to investigate XRD line broadening, the Scherrer method is a simplified formulation and therefore still employed to estimate the "apparent" domain sizes of physically broadened peak profiles. This method defines the crystallite size in terms of

a mean effective size of the coherently scattering region normal to the reflecting planes. The Scherrer relation between crystallite size and integral breadth is given by

$$D_{hkl} = \frac{K\lambda}{\beta_{2\theta}\cos\theta}, \tag{3}$$

where K is Scherrer's constant which is subjected to the process of the width measurement, the size distribution, and the shape of the crystals. Generally, the numerical value of K for spherical crystallites is of ∼0.89, and $\beta_{2\theta}$ is the width of diffraction peak in radians at a height halfway between backgrounds.

To investigate the phase constitution at high temperature, annealing experiments were performed at a series of temperatures ranging from 300 to 900 °C with temperature steps of 100 °C under high vacuum (1.3×10^{-5} Pa). In each step the annealing time was fixed to 10 h. No phase transition was observed within this temperature range.

Film thicknesses were measured by automated surface profilometry (Ambios Technology XP-2 Stylus Profiler). For the mappings, a diamond tip was moved over the lift-off cross-areas of the photolithographically patterned substrates. A velocity of 100 µm/s was chosen and a constant load of 0.5 µg was applied. Surface topography images were acquired by AFM (Bruker Dimension) in Fastscan mode. To reduce potential alterations of the film, the non-contact mode was used. A scan size of 3 µm × 3 µm and a scan rate of 1 Hz were chosen. The surface roughness of as-deposited Nb–Mo–Ta–W film is shown in supporting information. For surfaces, whose roughness are characterized by a single length scale, roughness parameters were calculated by the arithmetic mean roughness Ra.

High-throughput electrical resistance measurements were carried out at room temperature, with the intention to efficiently identify compositional areas of interest in the libraries. For the case of formation of intermetallic phases along

a composition gradient, we would expect maxima or minima in the resistivity gradient, whereas in the case of complete miscibility (solid solutions), at least for binary systems, the resistivity values should increase for increasing amounts of the second element, leading to a maximum of resistivity for intermediate compositions of the solid solution [24]. A custom-built test stand [23] was used to perform automated measurements by means of a four-point probe measurement head. A LabVIEW-based program was applied to control the automated routine to cover all 342 MAs. A current I_0 of 80 mA was chosen, and each MA was measured three times. The value of resistivity (ρ) for each MA was calculated by assuming a cylindrical expansion of the electrical field in the thin film. Under this assumption, the electrical field is confined to radially with a length equal to the film thickness, and the resistivity could be determined from the following equation,

$$\rho = \frac{\pi}{\ln 2} \cdot t \cdot R,$$

where R and t are resistance and film thickness, respectively. R is obtained directly from our four-point probe measurement.

High-throughput nanoindentation was carried out using a nanoindenter (Ti 900 of Hysitron, modified with a Performech 2 advanced control module). In a typical measurement, a standard Berkovich tip was used which was held for 5 s at a maximum load of 2000 μN for mapping measurements, followed by around 10 s for tip loading and unloading. The indentation size $h(\max)$ is about 70–100 nm for each indent. Here, $h(\max)$ means the largest distance between top and surface. In each MA, a 100 μm × 100 μm rectangle containing 9 measurement points (forming a pattern of 3 × 3) was measured.

Results and Discussion

Composition Analysis

EDS analysis for the as-deposited Nb–Mo–Ta–W ML shows a continuous composition spread across the wafer for all constituent elements. The ML has a center composition of $Nb_{39}Mo_{18}Ta_{22}W_{21}$, which was chosen based on an initial simulation result. The relative elemental compositions at each of the 342 MAs are shown in a pie chart diagram in Fig. 1b. In each pie chart, the arc length of a slice is proportional to the element content it represents. Figure 2a shows the corresponding composition ranges in a color-coded scatter diagram for Nb, Mo, Ta, and W, respectively. Within the 342 MAs, the Nb content ranges from 20 to 59 at.%, Mo from 9 to 31 at.%, Ta from 10 to 42 at.%, and W from 12 to 32 at.%. Based on this, the complete composition range of
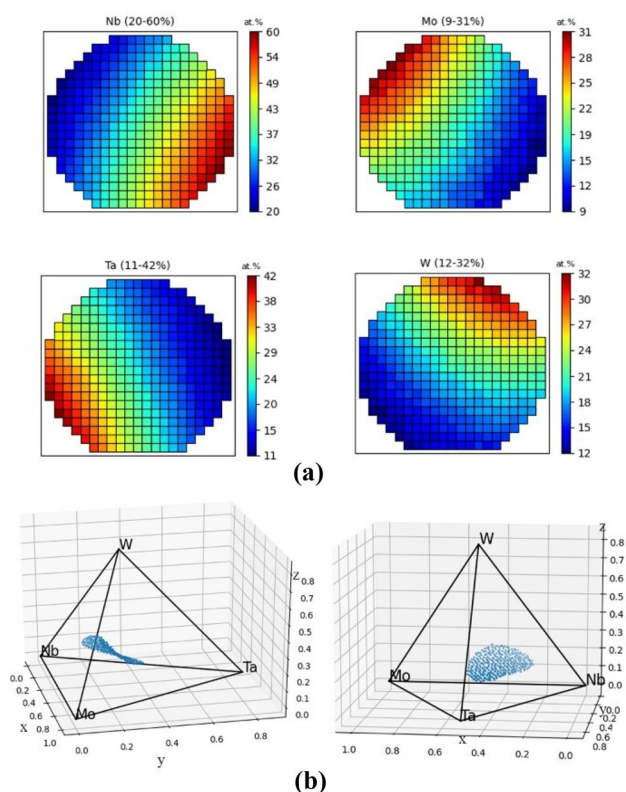

Fig. 2 a Color-coded diagrams show the element content for Nb, Mo, Ta, and W, respectively. The composition spread is $Nb_{20-59}Mo_{9-31}Ta_{10-42}W_{12-32}$ and the center composition is $Nb_{39}Mo_{18}Ta_{22}W_{21}$. **b** Visualization of the covered compositions of the material library $Nb_{20-59}Mo_{9-31}Ta_{10-42}W_{12-32}$ in the quaternary composition space, plotted in different viewing angles. Each vertex in the tetrahedron corresponds to the content of the respective element. The transformation from tetrahedral four-component coordinates into 3D Cartesian coordinates is performed according to the algorithms in Ref. [25] (Color figure online)

the ML can be written as $Nb_{20-59}Mo_{9-31}Ta_{10-42}W_{12-32}$ and the corresponding composition spread is shown in Fig. 2b.

Structural Properties

The XRD patterns determined on the Nb–Mo–Ta–W ML are similar for all 342 MAs, showing a bcc structure. All compositions have preferred orientations of (110), (200), (211), (200), and (310), located at 2θ of around 39°, 56°, 70°, 84°, and 97°, respectively (see Fig. 3). This indicates that the films are nanocrystalline and crystallographically textured. A strong (110) texture was observed using EBSD with a constructed pole figure [26]. The observed XRD patterns match well with those of metallic Ta (ICSD-167903) and can be assigned to the bcc structure. There is no other phase detected such as B2 (ordered bcc) and no diffraction peaks corresponding to impurities. The calculated lattice constants and crystallite sizes are shown in Fig. 4.

Fig. 3 XRD patterns of the Nb–Mo–Ta–W thin-film ML. **a** All selected patterns (from left bottom to right top) show exclusively a single-phase bcc structure. The calculated structural parameters and the corresponding compositions from selected diffraction patterns are listed in Table SI2. **b** Quasi-linear shifts of the (110) peak position along the different gradients
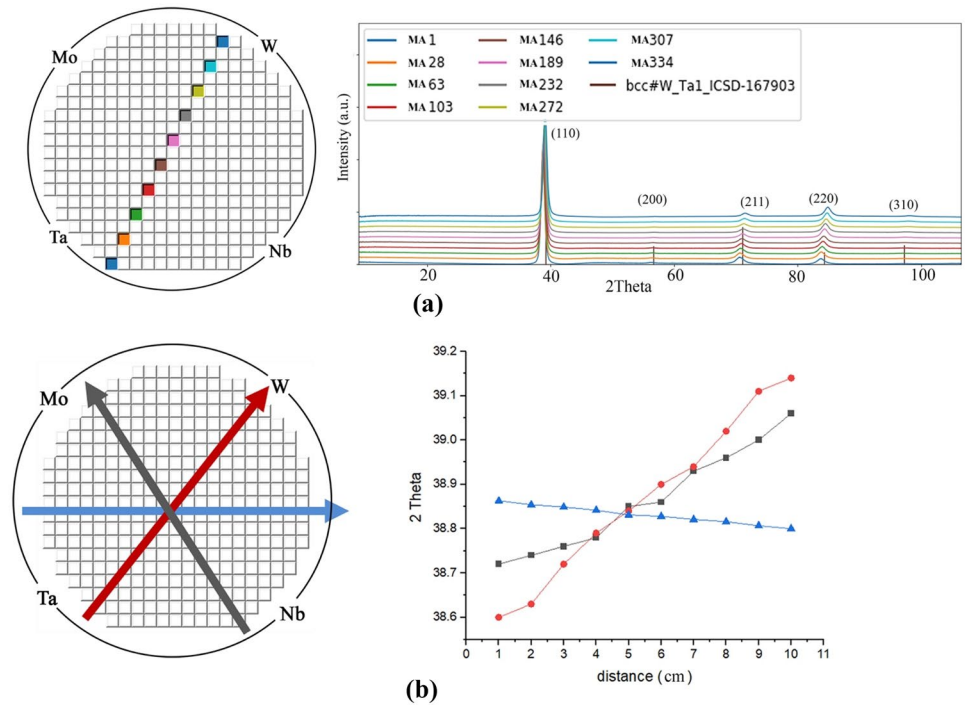
Fig. 4 Lattice constants and crystallite sizes of the as-deposited Nb–Mo–Ta–W films shown in color code across the ML (Color figure online)
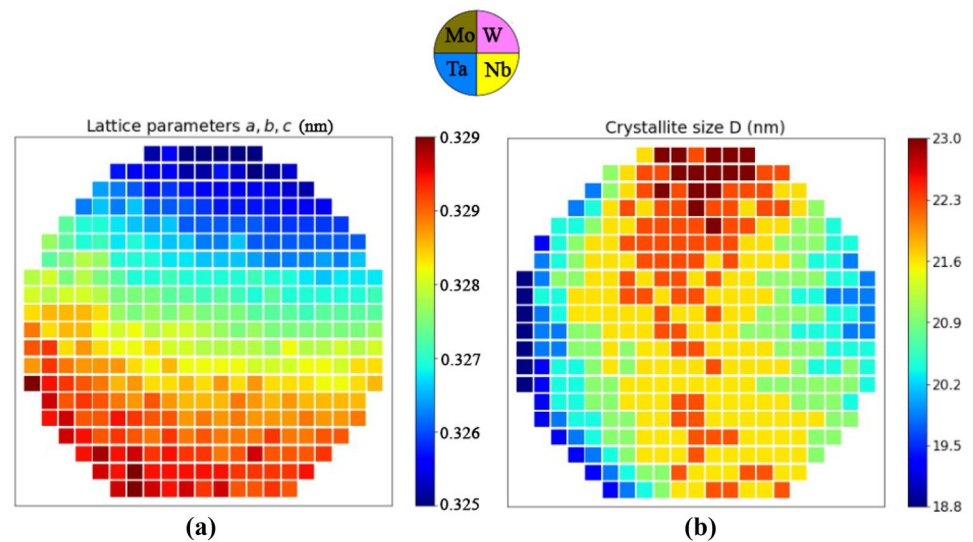
Subsequently, the influence of annealing temperature on the phase transformation of Nb–Mo–Ta–W ML was studied. No obvious changes of the XRD pattern was detected after annealing the ML up to 900 °C in vacuum. The observation that the bcc phase is present for all compositions of the ML, independent of annealing temperature, indicates that the system Nb–Mo–Ta–W has a high compositional tolerance that enables it to be stabilized in a wide compositional range while maintaining the same crystal structure.

In order to elucidate the composition–structure relationship in more detail, a group of MAs across the Nb–Mo–Ta–W ML along the bottom left to top right direction was selected as a representative composition regime for further discussion; the MAs across other film directions are given in the Supporting Information.

The corresponding XRD patterns in this direction are shown in Fig. 3. The obtained values for the spacings of the specific lattice planes $d(hkl)$ and the lattice constants, together with the related crystallite size and compositions, are summarized in Table SI2. The gradual change of the lattice constants from 0.325(4) to 0.319(7) nm indicates the presence of a solid solution state in the fabricated ML. The calculated lattice constants are in good agreement

with those estimated by the linear combination of pure elements from Vegard's law [27].

The W content increases steadily from bottom left to right top of the ML (see Table SI2). Following this direction, the peak positions shift to higher 2θ values, and accordingly, the lattice constants decrease from 0.325(4) nm for $Nb_{23}Mo_{18}Ta_{43}W_{16}$ (MA #1) to 0.319(7) nm for $Nb_{23}Mo_{20}Ta_{17}W_{40}$ (MA #334). The observed shift matches a linear rule of mixture in terms of Vegard's law, i.e., a net lattice constant calculated as a fractional additive sum of the lattice constants of the individual elements in bcc lattice structure [28, 29]. Table SI3 lists the peak positions of Nb, Mo, Ta, and W from the Pauling File database [25, 30–34]. The table shows that the XRD peaks for both Mo and W are located at relatively higher 2θ values than those of Ta and Nb. Consequently, due to solid solution mixing, the resulting W- and Mo-rich regions (right side of ML) essentially possess higher 2θ values compared to Ta- and Nb-rich regions (left side of ML). This example shows that the lattice constants for the different Nb–Mo–Ta–W compositions in the ML correspond to the average values of its constituent elements, weighted by composition

fraction. Note that the composition gradients result from the geometric arrangement of the sputter sources.

Analysis of Thickness and Electrical Properties

The mapping of film thickness t for all 342 MAs is visualized in Fig. 5a and b and in Fig. SI3. These thickness values range from 1193 to 1306 nm, and the mean value being around 1210 nm. The obtained film thickness is high enough to avoid mechanical effects from the substrate and is suitable for nanoindentation tests. Further EDX analyses indicate that the film thickness correlates with the Nb gradient, i.e., the thickness value increases as the Nb content increases. This is explained by the larger volume required for deposited Nb. Table SI4 shows that the variation of molar volumes for different constituent metals in Nb–Mo–Ta–W ML is notable, ranging from 9.38 for Mo to 10.83 m^3/mol for Nb.

Figure 5c shows the resistivity map for the Nb–Mo–Ta–W ML. The full set of resistivity values for each MA is included in Supporting Information Fig. SI5. The obtained resistivity for each MA is higher than the simple average of its constituent elements. For example, the element Mo has the lowest nominal resistivity (only 52 nΩ m, see Table SI4)

Fig. 5 **a** Color-coded film thickness map of the ML. **b** Distribution of thickness values for all 342 MAs. **c** Resistivity map of as-deposited Nb–Mo–Ta–W ML. Electrical resistivity values were calculated by assuming a cylindrical expansion of the electrical field in thin films. For calculation see Ref. [35]. **d** Resistivity values along different gradients in the ML (Color figure online)

(a)

(b)

(c)

(d)
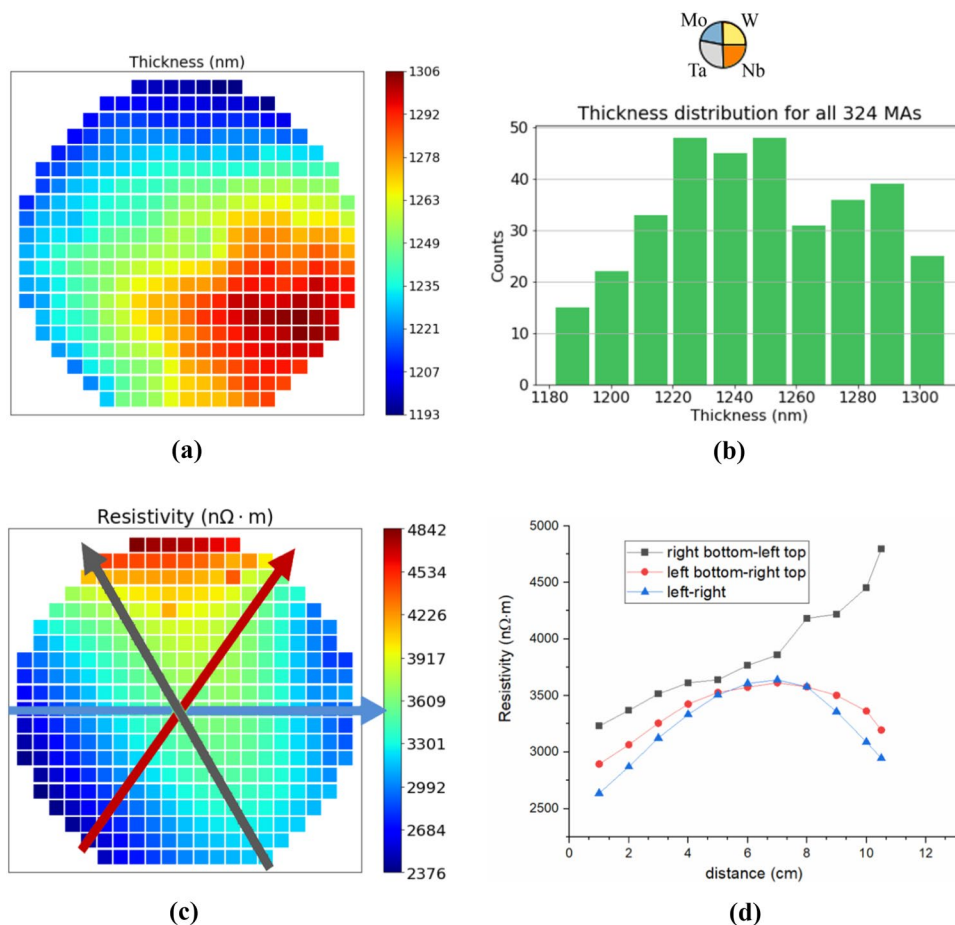
among the four constituent elements. However, a high value of around 4000 nΩ m is observed in the Mo-rich region. The resistivity values decrease to around 2000 nΩ m along the left side of the ML region with high-Ta content of around 40 at.%. Resistivity values change more abruptly in the high-W content region (from around 3500 to 2200 nΩ m) than in the high-Ta region (from around 2800 to 2200 nΩ m). Figure 5d shows the values of resistivity along different composition gradients in the ML. The results show a behavior indicating the solid solution state of the films.

Analysis of Mechanical Strength and Its Optimization

Figure 6a shows the distribution of the predicted uniaxial yield stress σ_y using the Maresca–Curtin model [20] for mechanical strength parameterized using experimental data for pure elements as outlined in the Materials and Methods section. The data points in Fig. 6a are based on the experimentally measured compositions displayed in Fig. 2a and show a clear increase toward the Mo-rich region in the upper left corner of the ML. For comparison,

the distributions of the experimentally measured hardness and reduced modulus are shown in Fig. 6b and c. For all of them, an increase toward regions with Mo–W-rich compositions in the upper part of the ML are observed, see Fig. 7. For a more detailed comparison of these values, three pair plots are shown in Fig. 6d–f. The positive monotonic correlation between the analytically predicted uniaxial yield stress σ_y and the experimentally measured hardness and reduced modulus values is clearly established. This supports the validity of using calculated values of σ_y as a function of proxy property for optimization of the mechanical strength of bcc RHEA, so the absolute value does not play a direct role, but only the direction of ascending trend in composition space is important.

We further performed a non-linear fit of our experimentally measured values of hardness and reduced modulus vs. the predicted uniaxial yield stress σ_y and identified the confidence intervals, also shown in Fig. 6d and e. We can only speculate about the origin of the deviations between our experimental data and the predicted uniaxial yield stress σ_y. However, the scatter in the experimental data suggests that the largest part of the deviations between model and
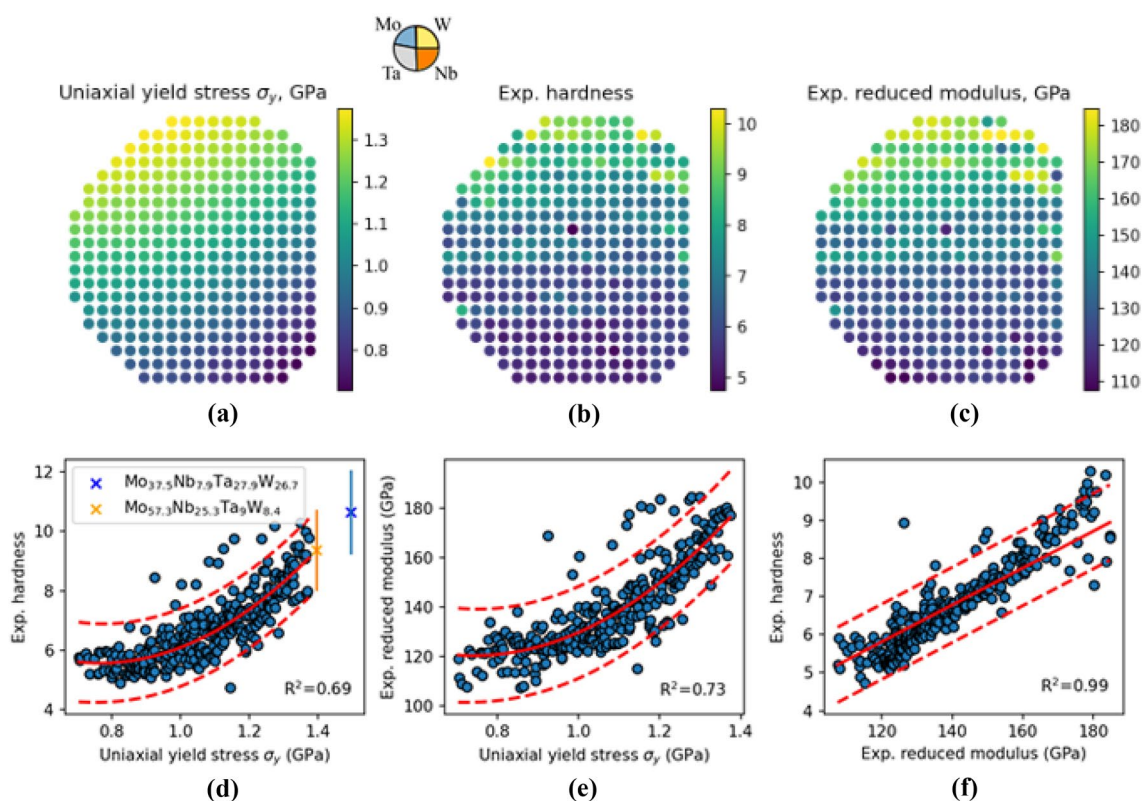
Fig. 6 **a** Uniaxial yield stress σ_y calculated using the Maresca–Curtin model, based on experimental lattice constant a, elastic moduli C_{11}, C_{12}, and C_{44}, and misfit volumes ΔV_j of the constituent elements, **b** experimentally measured hardness, **c** reduced modulus for the materials library, and **d**–**f** their corresponding pair correlations. Red solid and dashed lines show quadratic (**d**, **e**) and linear (**f**) fits and corresponding confidence intervals. R^2 metrics of the fits are also shown. Predicted hardness values and confidence intervals for two optimized compositions are shown on the panel (**d**) with crosses

Fig. 7 Color-coded dependencies of experimentally measured hardness and reduced modulus along different directions on the ML (Color figure online)
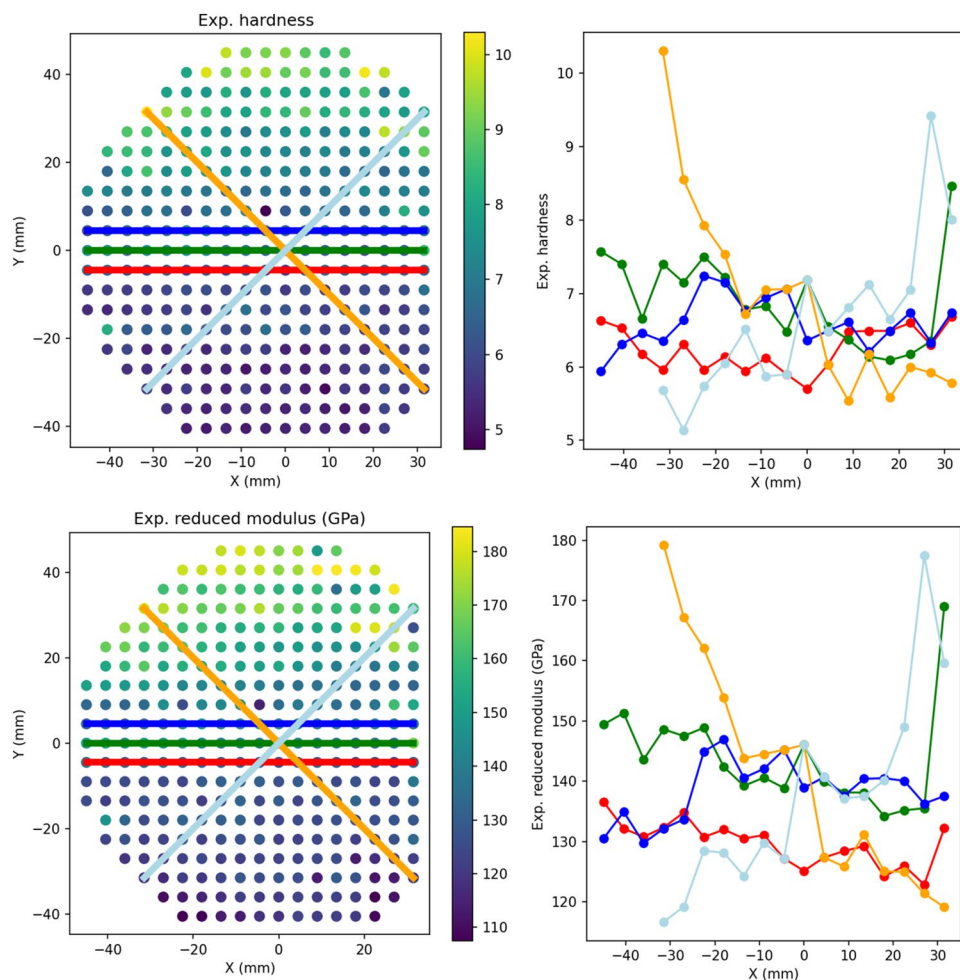
experiment is directly related to noise and uncertainty in the experiments.

In Ref. [22] an optimization of Mo–Nb–Ta–W alloys to maximize yield stress predicted by the Maresca–Curtin model was conducted and a new composition $Mo_{37.5}Nb_{7.9}Ta_{27.9}W_{26.7}$ was proposed. Both Mo and W have larger elastic moduli than Nb and Ta, while they also have smaller atomic volumes. Thus, mixing Mo and W with Ta increases atomic volume difference, but preserves a large average elastic modulus, thereby increasing yield strength.

In this work we performed an additional optimization to maximize the uniaxial yield stress σ_y divided by mass density ρ. The correspondingly optimized composition $Mo_{57.3}Nb_{25.3}Ta_9W_{8.4}$ has a comparatively slightly smaller uniaxial yield stress, but a much lower density, as shown in Fig. 8. Thus, based on this study and after validation by help of the Maresca–Curtin model for the yield stress as a reasonable measure for the materials' mechanical strength, derived from its hardness and solid solution state, we
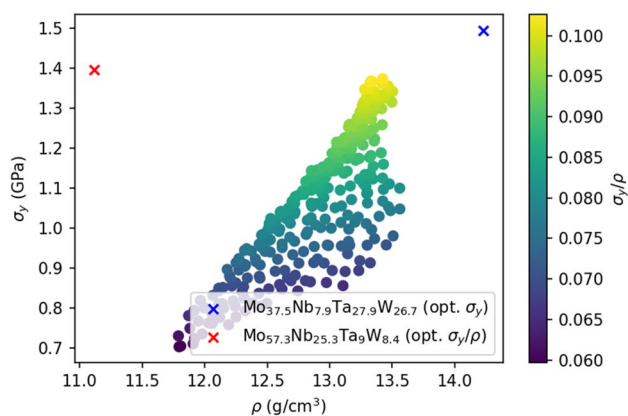
Fig. 8 Uniaxial yield stress σ_y predicted by Maresca–Curtin model based on experimental lattice constant a, elastic moduli C_{11}, C_{12}, and C_{44}, and misfit volumes ΔV_j of the constituent elements and density estimated by rule of mixtures for samples from RHEA ML. The σ_y/ρ values are shown by color. Two optimized compositions are shown with cross symbols (Color figure online)

propose a new RHEA composition that indicates a better strength-to-density ratio. The predicted hardness and confidence interval are shown in Fig. 6d. Further high-throughput synthesis of RHEA in a surrounding composition space would allow covering not only the exact optimized composition, but also nearby regions, which would help to compensate for approximations that we made in the prediction of the uniaxial yield stress σ_y.

Conclusion

A quaternary thin-film RHEA materials library comprising the composition range $Nb_{20-59}Mo_{9-31}Ta_{10-42}W_{12-32}$ was fabricated by combinatorial co-sputtering from four elemental sources. The correlation between compositions with resulting structures and hardness was studied. The results show that all compositions led to alloys with bcc structure. We found that compositions with high Mo contents provide the highest hardness values. The observed high compositional variability, which allows for the easy formation of bcc solid solutions by accommodating a wide range of constituent elements, enables the application of the Maresca–Curtin analytical model for the calculation of the mechanical uniaxial yield stress, based on experimental lattice constant a, elastic moduli C_{11}, C_{12}, and C_{44}, and misfit volumes ΔV_j of the constituent elements. The considered model does not include such effects as direct solute–solute interactions, short-range order and segregation, and the predicted yield strength is not directly proportional to the experimentally measured hardness, therefore some disagreement between analytical predictions and experimental measurements must be expected. However, the comparison of the model predictions with measured hardness values demonstrates a strong positive correlation and thus practically enables the use of the analytical model as a validated proxy for further optimization of a bcc RHEA's composition with high mechanical strength in a continuous composition range. Thus, the compositional design principle, based on the use of an experimentally validated proxy property (analytical yield strength) for the target property (hardness) optimization was demonstrated in this paper.

Author Contributions Conceived and designed the experiments: BX, RD, and AL. Performed the experiments: BX, AS, HB, and JM. Analyzed the data: BX, YL, and RD. Contributed reagents/materials/analysis tools: YL, AS, and DR. Wrote the paper: BX, YL, and AL.

Declarations

Conflict of interest No conflict of interest exits in the submission of this manuscript, and manuscript is approved by all authors for publication. I would like to declare on behalf of my co-authors that the work described was original research that has not been published previously, and not under consideration for publication elsewhere, in whole or in part. All the authors listed have approved the manuscript that is enclosed.

References

1. M.-H. Tsai, J.-W. Yeh, High-entropy alloys: a critical review. Mater. Res. Lett. **2**(3), 107–123 (2014)
2. M.-H. Chuang, M.-H. Tsai, W.-R. Wang, S.-J. Lin, J.-W. Yeh, Microstructure and wear behavior of AlxCo1.5CrFeNi1.5Tiy high-entropy alloys. Acta Mater. **59**(16), 6308–6317 (2011)
3. C.-W. Tsai, M.-H. Tsai, J.-W. Yeh, C.-C. Yang, Effect of temperature on mechanical properties of Al0.5CoCrCuFeNi wrought alloy. J. Alloys Compd. **490**(1), 160–165 (2010)
4. Y.J. Zhou, Y. Zhang, Y.L. Wang, G.L. Chen, Solid solution alloys of AlCoCrFeNiTix with excellent room-temperature mechanical properties. Appl. Phys. Lett. **90**(18), 181904 (2007)
5. O.N. Senkov, G.B. Wilks, J.M. Scott, D.B. Miracle, Mechanical properties of Nb25Mo25Ta25W25 and V20Nb20Mo20Ta20W20 refractory high entropy alloys. Intermetallics **19**(5), 698–706 (2011)
6. A. Poulia, E. Georgatis, A. Lekatou, A. Karantzalis, Microstructure and wear behavior of a refractory high entropy alloy. Int. J. Refract. Met. Hard Mater. **57**, 50–63 (2016)
7. Y. Wu, Y. Cai, T. Wang, J. Si, J. Zhu, Y. Wang, X. Hui, A refractory Hf25Nb25Ti25Zr25 high-entropy alloy with excellent structural stability and tensile properties. Mater. Lett. **130**, 277–280 (2014)
8. D.B. Miracle, J.D. Miller, O.N. Senkov, C. Woodward, M.D. Uchic, J. Tiley, Exploration and development of high entropy alloys for structural applications. Entropy **16**(1), 494–525 (2014)
9. O.N. Senkov, S.V. Senkova, D.M. Dimiduk, C. Woodward, D.B. Miracle, Oxidation behavior of a refractory NbCrMo0.5Ta0.5TiZr alloy. J. Mater. Sci. **47**(18), 6522–6534 (2012)
10. Y. Zou, S. Maiti, W. Steurer, R. Spolenak, Size-dependent plasticity in an Nb25Mo25Ta25W25 refractory high-entropy alloy. Acta Mater. **65**, 85–97 (2014)
11. O. Senkov, G. Wilks, D. Miracle, C. Chuang, P. Liaw, Refractory high-entropy alloys. Intermetallics **18**(9), 1758–1765 (2010)

12. C.-C. Juan, M.-H. Tsai, C.-W. Tsai, C.-M. Lin, W.-R. Wang, C.-C. Yang, S.-K. Chen, S.-J. Lin, J.-W. Yeh, Enhanced mechanical properties of HfMoTaTiZr and HfMoNbTaTiZr refractory high-entropy alloys. Intermetallics **62**, 76–83 (2015)

13. M. Wang, Z. Ma, Z. Xu, X. Cheng, Microstructures and mechanical properties of HfNbTaTiZrW and HfNbTaTiZrMoW refractory high-entropy alloys. J. Alloys Compd. **803**, 778–785 (2019)

14. O.A. Waseem, H.J. Ryu, Combinatorial synthesis and analysis of $Al_xTa_yV_z$-$Cr_{20}Mo_{20}Nb_{20}Ti_{20}Zr_{10}$ and $Al_{10}CrMo_xNbTiZr_{10}$ refractory high-entropy alloys: oxidation behavior. J. Alloys Compd. **828**, 154427 (2020)

15. H. Chen, A. Kauffmann, S. Laube, I.-C. Choi, R. Schwaiger, Y. Huang, K. Lichtenberg, F. Müller, B. Gorr, H.-J. Christ, Contribution of lattice distortion to solid solution strengthening in a series of refractory high entropy alloys. Metall. Mater. Trans. A **49**(3), 772–781 (2018)

16. N. Guo, L. Wang, L. Luo, X. Li, R. Chen, Y. Su, J. Guo, H. Fu, Microstructure and mechanical properties of in-situ MC-carbide particulates-reinforced refractory high-entropy $Mo_{0.5}NbHf_{0.5}ZrTi$ matrix alloy composite. Intermetallics **69**, 74–77 (2016)

17. O.N. Senkov, J.M. Scott, S.V. Senkova, D.B. Miracle, C.F. Woodward, Microstructure and room temperature properties of a high-entropy TaNbHfZrTi alloy. J. Alloys Compd. **509**(20), 6043–6048 (2011)

18. O.N. Senkov, D.B. Miracle, K.J. Chaput, J.P. Couzinie, Development and exploration of refractory high entropy alloys—a review. J. Mater. Res. **33**(19), 3092–3128 (2018)

19. A. Roh, D. Kim, S. Nam, D.-I. Kim, H.-Y. Kim, K.-A. Lee, H. Choi, J.-H. Kim, NbMoTaW refractory high entropy alloy composites strengthened by in-situ metal-non-metal compounds. J. Alloys Compd. **822**, 153423–153423 (2020)

20. F. Maresca, W.A. Curtin, Mechanistic origin of high strength in refractory BCC high entropy alloys up to 1900K. Acta Mater. **182**, 235–249 (2020)

21. H. Ledbetter, S. Kim, Monocrystal elastic constants and deprived properties of the cubic and the hexagonal elements, in *Handbook of Elastic Properties of Solids, Fluids, and Gases*. ed. by M. Levy, H.E. Bass, R.R. Stern (Academic, San Diego, 2001)

22. A. Ferrari, Y. Lysogorskiy, R. Drautz, Design of refractory compositionally complex alloys with optimal mechanical properties. Phys. Rev. Mater. **5**(6), 063606 (2021)

23. S. Thienhaus, S. Hamann, A. Ludwig, Modular high-throughput test stand for versatile screening of thin-film materials libraries. Sci. Technol. Adv. Mater. **12**(5), 054206–054206 (2011)

24. S. Thienhaus, D. Naujoks, J. Pfetzing-Micklich, D. König, A. Ludwig, rapid identification of areas of interest in thin film materials libraries by combining electrical, optical, X-ray diffraction, and mechanical high-throughput measurements: a case study for the system Ni–Al. ACS Comb. Sci. **16**(12), 686–694 (2014)

25. T. Shimura, A.I.S. Kemp, Am. Mineral. **100**, 2545 (2015)

26. Yu. Yuan Xiao, H.M. Zou, A.S. Sologubenko, X. Maeder, R. Spolenak, J.M. Wheeler, Nanostructured NbMoTaW high entropy alloy thin films: High strength and enhanced fracture toughness. Scr. Mater. **168**, 51–55 (2019)

27. L. Vegard, Die Konstitution der Mischkristalle und die Raumfüllung der Atome. Z. Phys. **5**(1), 17–26 (1921)

28. K. Jacob, S. Raj, L. Rannesh, Vegard's law: a fundamental relation or an approximation? Int. J. Mater. Res. **98**(9), 776–779 (2007)

29. W. Li, M. Pessa, J. Likonen, Lattice parameter in GaNAs epilayers on GaAs: deviation from Vegard's law. Appl. Phys. Lett. **78**(19), 2864–2866 (2001)

30. P. Villars, M. Berndt, K. Brandenburg, K. Cenzual, J. Daams, F. Hulliger, T. Massalski, H. Okamoto, K. Osaki, A. Prince, The pauling file. J. Alloys Compd. **367**(1–2), 293–297 (2004)

31. J.W. Edwards, R. Speiser, H.L. Johnston, High temperature structure and thermal expansion of some metals as determined by X-ray diffraction data. I. Platinum, tantalum, niobium, and molybdenum. J. Appl. Phys. **22**(4), 424–428 (1951)

32. A. Arakcheeva, G. Chapuis, H. Birkedal, P. Pattison, V. Grinevitch, The commensurate composite [sigma]-structure of [beta]-tantalum. Acta Crystallogr. Sect. B **59**(3), 324–336 (2003)

33. A. Friedrich, B. Winkler, L. Bayarjargal, E.A. Juarez Arellano, W. Morgenroth, J. Biehler, F. Schröder, J. Yan, S.M. Clark, In situ observation of the reaction of tantalum with nitrogen in a laser heated diamond anvil cell. J. Alloys Compd. **502**(1), 5–12 (2010)

34. E.R. Jette, F. Foote, Precision determination of lattice constants. J. Chem. Phys. **3**(10), 605–616 (1935)

35. B. Xiao, X. Wang, A. Savan et al., Phase constitution of the noble metal thin-film complex solid solution system Ag-Ir-Pd-Pt-Ru in dependence of elemental compositions and annealing temperatures. Nano Res. **15**, 4827 (2021)